Observations of fire intensity and fire spread rate—RxCADRE 2012

B. Butler[A,D], C. Teske[B], D. Jimenez[A], J. O'Brien[C], P. Sopko[A], C. Wold[A], M. Vosburgh[A], B. Hornsby[C], and E. Loudermilk[C]

[A]US Forest Service, Rocky Mountain Research Station, Fire Sciences Laboratory, Missoula MT
[B]Center for Landscape Fire Analysis, The University of Montana, Missoula MT
[C]US Forest Service, Southern Research Station, Athens Fire Laboratory, Athens, GA
[D]Corresponding author. Email: bwbutler@fs.fed.us

Abstract

Radiant and convective heating and cooling were measured approximately 0.5 m above the ground surface in nine prescribed fires (eight in grass units and one in a long leaf pine forested unit), measurements from two of the burn blocks are reported here. Flame heights varied from 0.3 to 1.8 m, flaming zone depth varied from 0.3 to 3 m. Fire rate of spread derived from observations of fire spread rate between sensors was 0.1 to 0.48 m/s. Rate of spread derived from ocular estimates reached 0.51 m/s for heading fire and 0.25 m/s for backing fire. Measurements of radiant and total energy incident on the sensors at the time of peak flame presence reached 18.8 and 36.7 kW/m2 respectively. Peak air temperatures reached 1159°C. Calculated fire radiative energy varied from 7 to 162 kJ m^{-2} and fire total energy varied from 3 to 2 kJ m^{-2}. Measurements of flame emissive power peaked at 95 kW m^{-2}. Horizontal air flow in the direction of flame spread immediately prior to, during, and shortly after the flame arrival reached 4.6 m s^{-1}, vertical velocities varied from 62 m s^{-1} downward flow to 4.4 m s^{-1} upward flow.

Summary

Measurements of fire intensity, flame geometry and rate of spread using several methods are compared. Measurement uncertainty and variability is explored.

Keywords: fire behavior, fire modeling, field measurements, energy transport

Introduction

Energy transfer drives wildland fire intensity and rate of spread (Anderson 1969; Yedinak, *et al.* 2006; Anderson 2009). Quantification of energy transport on wildland fires is a critical yet poorly documented element of wildland fire science especially the variability in space and time as well as the proportion released through radiant and convective heating modes (Frankman *et al*. 2012*a*). While radiative energy transport has received the bulk of the interest in wildland fire research, recent studies have focused on understanding the role of both radiative and convective energy transport to wildland fire ignition and spread (Morandini and Silvani 2010; Yedinak *et al*. 2010). For example, the radiometric properties of the energy emitted from wildland flames has been of particular interest (Parent et al. 2010) as well as analysis of heat flux measurement uncertainty in flames (Bryant *et al.* 2003; Pitts *et al.* 2005). However, understanding of the properties of energy transfer in wildland flames is still limited (Sacadura 2005; Viskanta 2008; Finney *et al.* 2010) likely due to logistics associated with sensor deployment, the high temperature environment, and the natural variability in fire intensity over time and space. When considering relationships between energy transport in wildland flames and particle ignition it is unclear how woody particles respond to temporal fluctuations in the heating source. An analytical solution to small particle heating (Frankman 2009) demonstrates that particle time to ignition is related to both the periodicity and the magnitude of the heating source. It also shows that these two factors are directly correlated (*i.e.* lower frequency signals result in ignition at lower magnitudes). Thus the temporal characteristics of the heating regime are relevant to additional understanding of wildland fire. To understand and accurately predict the behavior of forest fires (Albini 1996), model fire emissions (Wooster *et al.* 2005; Freeborn *et al.* 2008), and improve public and wildland firefighter safety (Butler and Cohen 1998; Butler 2014), it is critical to understand how energy is released from burning wildland fires.

Studies have explored energy transport in wildland fires for the past century, but it is only in the past decade that significant progress has been made on this topic. Radiative heating magnitudes present in wildland fires have been measured as high as 300 kW m^{-2} (Butler 2003; Butler *et al.* 2004; Frankman *et al.* 2012*a*). Only a limited number of measurements of convective heating have been reported. In general, the data indicate that convective heating alternates between heating and cooling with peak magnitudes between 22 and 140 kW m^{-2} (under ideal flame spread conditions). The convective heat flux is characterized by rapid fluctuation between positive and negative convection values owing to alternating packets of cool air intermingled with hot combustion products. There is still much that is not understood, with respect to energy transport in fires burning natural fuels, for example how does the relative contribution of radiant and convective heating vary with vegetation and burning environment, what are the temporal characteristics of each, does the contribution of each vary through the burning period, how does each contribute to ignition and fire spread, does fire energy release relate to emissions production, and if so in what way? Recognizing the need for additional understanding into energy transport in fires the RxCADRE project was initiated to collect a comprehensive set of data that address the critical research needs (Ottmar *et al.* In review). The data collected in this effort will support future development of wildland fire behavior models, emissions predictions, and vegetation response to fire. This document focuses on the ground based video cameras and sensors that characterize energy transport at or within 1 m of the ground surface. Here we report fire type, flame geometry, rate of spread, energy measurements, and fire type (i.e. heading, flanking, backing). Specifically, time-resolved convective and radiative heat fluxes, air temperatures, vertical and horizontal velocities and flame emissive power from fires burning in two vegetation types are discussed. Calculated values include flame radiative energy and flame convective energy. The focus of the sensors deployed by this team was to correlate and generalize fire energy release and intensity with respect to the fire, fuel, and environmental conditions. This data can be used to develop a new understanding about the relative contribution of radiative and convective heating to overall energy transport in and around wildland fires under a variety of conditions and inform the characterization of emissions from wildland fires.

Methods

Fire sensors

A system consisting of temperature, air flow, and energy sensors for quantifying energy and mass transport in wildland fires was used to characterize the effect of treatment on fire spread and intensity (Butler and Jimenez 2009) (Butler and Jimenez 2009). The system consists of two types of enclosures: a sensor/datalogger combination mounted in an aluminum housing that allows *in-situ* characterization of convective/radiant energy transport in wildland fires and a video camera enclosure. This housing, termed the fire behavior package (FBP), measures 27 cm by 15 cm by 18 cm and weighs approximately 5.3 kg. It contains rechargeable batteries, a programmable datalogger, heat flux sensors, and other electronics. The standard FBPs consist of a Medtherm Dual Sensor Heat Flux sensor (Model 64-20T) provide incident total and radiant energy flux, a type K fine wire thermocouple (nominally 0.025 mm diameter wire), a custom designed narrow angle radiometer (NAR) (Butler 1993), and two pressure-based flow sensors (McCaffrey and Heskestad 1976). The sensors were calibrated prior to deployment as described elsewhere (Butler and Jimenez 2009). Convective heat flux at the sensor face can be estimated (Frankman *et al*. 2012*a*). Integration of the heat flux time histories can provide a measure of fire total, radiative and convective energy per unit area as a function of heating time. A recent study has shown that, for sampling rates less than 5 Hz, the difference between measured and actual peak radiative heating rates can be as great as 24% and on the order of 80% for 1-Hz sampling rates (Frankman *et al.* 2012*b*). The study also demonstrated that heating rates averaged over a 2 s period were insensitive to sampling rate across all ranges explored. In an effort to reduce measurement error all sensor data were recorded at 10 Hz.

The second part of the system is a fireproof enclosure housing a video camera (Jimenez *et al.* 2007). The camera system measures 10 cm by 18 cm by 19 cm and is constructed of 1.6 mm aluminum for a weight of approximately 1.8 kg. A double lens configuration of high temperature Pyrex© glass and a second lens of hot mirror coated glass (Edmund Optics) is mounted in the ports. This multi-layer dielectric coating reflects infrared radiation (heat), while allowing visible light to pass through. The preferred video camera model is the SONY PC-1000 HandyCam digital video camera; however other models can be substituted.

Typically each FBP is coupled with a camera for simultaneous recording of video and in-situ measurements allowing researchers to better evaluate fire behavior measurements relative to flame size and local spread rate. Visual analysis of the video images provides one method for measuring flame height, flame length, flame depth, flame angle, and fire rate of spread, provided that a calibration object is in the camera field-of-view. Both the FBP and camera enclosures are designed to be mounted on low cost tripods. Once mounted on the tripods the FBP and cameras are powered, and a single layer of 2.5-cm thick ceramic blanket and fiberglass reinforced aluminum foil material is wrapped around the box.

Fire behavior package layout

Fire behavior packages and in-fire video recorders were deployed on burn block S5 as shown in Fig. 1. The FBPs were located roughly along a transect parallel to the long axis of the burn block. Sensors and cameras were deployed in burn block L2G in the same vicinity as highly-instrumented plots (HIP) that were associated with measurements by others (see other reports in this issue). In all cases the FBPs were positioned to sense fire from the expected spread direction based on wind direction, terrain slope, and lighting procedures. Typically one camera and one to two FBPs were paired and deployed together. The cameras were oriented to provide images of the fire as it approached and burned over the respective FBPs; that is, cameras "looked" toward an FBP in an angle perpendicular to expected fire spread. All FBPs and cameras were located nominally 1.0 m above the mineral soil. The cameras and FBPs were oriented to "look" horizontally in the direction they were faced, the FBPs towards the expected fire and the cameras obliquely to the fire spread direction. The thermocouples sensed air temperature nominally 1.0 m above ground level. Narrow angle radiometers were included that looked horizontally towards the direction faced by the FBP and sensed energy emitted from a nominally 7 degree field of view.

Data analysis

Incident, radiant, and total heat flux at the surface of the FBP were evaluated to determine convective heating at the sensor face (Frankman *et al.* 2010). The fine wire thermocouple has a response time of approximately 0.01 s (Omega, n.d.) and was used to sense flame presence and flame residence time. Flame arrival at the FBP was indicated by a nearly vertical increase (~3000 to 5000°C s^{-1}) in temperature to several hundreds of degrees above ambient. This temperature increase was almost always associated with a nearly instantaneous increase in heat flux at the sensor (10 to 100 kW m^{-2} s^{-1}). The completion of the flame event was indicated by a rapid decay in air temperature. In some cases the thermocouple failed, in which case the radiometer data alone was used to gauge the arrival and completion of flaming combustion. Flame radiative and convective energy were calculated by integrating the respective signals over the period of flaming combustion.

Flame geometry

Flame geometry (i.e. flame height, flame length, flame depth and flame angle) was determined by visual observation of in-situ video images. Each measurement represents a minimum of three observations derived from various video images. Due to the low intensity of the fire it was difficult to clearly distinguish fire presence and thus the measurement uncertainty associated with these data are expected to be high.

Rate of spread

Rate of spread (ROS) data were estimated using the three different methods. The first method estimates ROS based on ignition time, arrival of flame front at FBP, and distance between FBPs and ignition line. For burn block S5 tower mounted infrared video imagery was used to monitor the progress of the fire front and its arrival at the individual FBPs. The second method estimates ROS based on distance between FBPs and the time difference between flame arrival at each FBP as indicated by the sensed temperature or heat flux, and the third method is based on visual observations of in-fire video footage. Unit S5 was ignited using a line ignition, and the FBPs were arranged generally along a transect oblique to the ignition line (Fig. 1) so all three methods were applied to estimate rate of spread. For unit L2G, all-terrain vehicle terra torches were used to create a line ignition; however, the FBPs were not arranged as oblique transects (Figs. 2, 3) and therefore measurement of transit times between FBPs was not possible. Thus, only the first and third methods were used to estimate ROS in unit L2G.

Results

Characterization of fire intensity is dependent on the context for the measurements. For example, remote measurements such as those derived from aircraft or satellite based sensors would likely "see" a different value than ground based sensors. Similarly the orientation of ground based sensors likely contributes to the magnitude of energy measured. Total energy released from fires can be many times greater than that measured by ground based sensors (Wooster *et al.* 2005b). For the purposes of this investigation, energy emitted generally along or near the ground surface (within 1 to 5 m) is assumed to be the primary driving factor for fire spread.

For this study, fire intensity is characterized by visual observations of flame height, flame length, and flame depth; derived rate of spread values (based on visual observations of video footage, calculations based on infrared images, and fire time-of-arrival at fire behavior packages); air temperature measurements; total and radiant energy measured incident on the near ground in-fire sensors (FBPs); and derived values for fire radiative energy and fire convective energy.

Fire type

Table 1 presents general observations of fire behavior that occurred near the FBP sensors and cameras. An effort is made to distinguish heading from flanking and backing fire. Sensor malfunctions are noted. The observations indicate that in burn block S5 (Fig. 1) the fire arrived at the two sensors nearest the ignition line as a head fire. Subsequent sensors and cameras recorded lower intensities and suggested that the fire front was less organized and spread in several directions. Most of these sensors indicate lower energy release, rate of spread and flame size, which all suggest lower fire intensity at these locations.

The second burn block (L2G) (see Figs. 2, 3) was much larger than S5. For this burn the sensors were grouped around three individual HIPs. While the unit was selected for the uniformity of vegetation type, loading and distribution, there remained significant spatial variability in these values. The variability was indicated in the observations of fire spread and intensity. For example, in L2G HIP 1, head fire was indicated for the four sensors nearest the ignition line but flanking fire for the remaining three sensors. Observations in L2G HIP 2 suggest lower intensity fire at the FBP closest to the ignition line but generally head fire at all other sensors, while L2G HIP 3 seems to have burned with lower intensity and more sporadic fire behavior than the other two HIPs in the unit.

Flame geometry

Table 2 presents observations of flame geometry obtained from video camera images. Flame geometries were generally lower in S5 than L2G, with flame heights averaging 0.45 m and flame depth averages of 0.75 m. L2G HIP 1 showed an average flame height of 0.90 m and average flame depth of 1.30 m. L2G HIP 2 had an average flame height of 0.60 m and flame depth of 2.30 m. L2G HIP 3 showed an average flame height of 0.75 m and depth of 1.50 m. Due to the low intensity of the measurements, the values have a high level of variability as indicated by the standard deviation associated with each burn block.

Rate of spread

Table 3 presents rate of spread values derived from infrared images of fire spread, fire arrival times, and sensor locations for both burn blocks. All three methods were used for block S5. The three methods suggest overall spread rates of 0.24, 0.23 and 0.26 m s^{-1} for the three methods respectively, with an increase in the standard deviation in the sample method type. For example, the largest deviation occurs for the video derived values, which are subjective. The between-sensor values derived using the second method vary from 0.11 to 0.35 m s^{-1}. This can be seen in Fig. 4, which uses the ROS and peak intensity values to illustrate the variability of fire behavior and intensity between sensors.

For block L2G, only the first and last methods were used to determine ROS (e.g. ROS based on FBP flame arrival after ignition time, and ROS estimated from video images). This is due to the positioning of the FBPs in groups rather than along transects as well as the ignition pattern generated by the ignition method (Fig. 3). The agreement between the two methods is not nearly as close as that for S5. HIP 1 values are 0.23 and 0.40 m s^{-1} for the two methods; HIP 2 values are 0.44 and 0.36 m s^{-1}; and HIP 3 values are 0.23 and 0.42 m s^{-1} respectively. Variability in individual observations is lowest for HIP 2.

Energy measurements

Measurements of energy incident on the FBPs as a function of time or flame presence are presented as peak and average values for a period encompassing the duration of flaming combustion at the FBP location in Table 4. Fig. 5 is presented to provide context for the values. Table 4 presents the data in terms of burn block or plot, FBP identifier (FBP ID), peak radiant flux at the sensor (Q_R), peak convective heat flux at sensor (Q_c), peak measured total heat flux at sensor (Q_T), flame emissive power from narrow angle sensor (E_F), peak kinetic air temperature (T_{air}), flame residence time from heat flux data (t_{flame}), average radiative heat flux over flaming period ($\overline{Q_R}$), average convective flux over the flaming period ($\overline{Q_C}$), average total heat at sensor for flaming period ($\overline{Q_T}$), fire radiative energy (FRE), fire convective energy (FCE), and fire total energy (FTE). The left column of Fig. 5 presents observations from FBP7 for S5. The peak temperature was 860 °C however it was very short lived (Fig. 5a), lasting much shorter than 1 second. Peak radiant, convective, and total and heat fluxes were 3.6, 4.3, and 7.2 kW m^{-2}, respectively (Fig. 5*c*). Flame residence time was nominally 7 seconds. Average radiant, convective, and total energy fluxes at the sensor faces during the flame presence were 2.1, 1.7, and 3.8 kW m^{-2}, respectively (Fig. 5*e*). The right column of Fig. 5 presents values for selected sensor FBP 22 deployed on L2G HIP 1. The values are believed to represent those characteristic of a head fire. As shown, the peak magnitude in air temperature was 1159 °C (Fig. 5*b*). Peak heat fluxes at the sensor were 18.8 (radiant), 18.2 (convective), and 36.7 (total) kW m^{-2} (Fig. 5*d*). Average radiant, convective, and total heat fluxes during the flaming phase were 11.1, 7.8, and 19.3 kW m^{-2}, respectively. Peak fire total, radiative and convective energy per unit area were 261, 143, and 118 kW m^{-2} respectively (Fig. 5*f*).

Average peak temperature (*T*) for all FBPs in S5 was 682°C; average peak heat fluxes (*Q*) were 8.6, 3.7, and 5.5 kW m^{-2} (total, radiant, and convective respectively); and average flame residence time (t_{flame}) was 12.3 s. The overall average of the mean radiant, convective, and total heat fluxes during flame presence were 2.7, 2.3, and 4.9 kW m^{-2}, respectively (Table 4). Average Peak temperature for all FBPs in L2G was 805°C; average peak heat fluxes were 10.1, 10.6 and 20 kW m^{-2} (radiant, convective, and total, respectively); and average flame residence time was 10.0 s. The average mean radiant, convective, and total heat fluxes during flame presence were 6.8 (radiant), 3.8 (convective), and 10.4 (total) kW m^{-2} (Table 4). Average fire energy per unit area were 104, 68, and 38 kJ m^{-2}.

Discussion

Observations and metrics of flame size, fire spread rate and fire intensity suggest low intensity fire for both burns. The observations in Table 1 indicate that most FBPs in S5 were exposed to low intensity flanking fire. This is supported in overhead infrared images. L2G seems to have burned most uniformly in the vicinity of HIP 2. HIP 1 and HIP 3 observations indicate low intensity fire behavior and intensity, based on observations of the video images. Overall the sensor failure rate was low (nominally 4 out of 28 deployments).

Table 2 data relative to S5 suggest that the use of distance between FBP and ignition line provides the lowest measurement uncertainty, but shows little of the variability of ROS. Estimates based on distance and time of spread between FBPs provides a metric of local variability in fire spread rate. Estimates obtained from observation of video images show the greatest measurement uncertainty (standard deviation) but the average is within 13% of the averages obtained from the other two methods. The data suggest that rate of spread if based on one or two local measurements should be associated with significant uncertainty; however, averaging measurements based on four or more nearby but separate observations when averaged are within 13% of overall average spread rates. This trend however is not fully supported by the observations associated with L2G. For these data it appears that the greatest variability is associated with the observations of fire variability from video images. For example, HIP 2 had the most observations of head fire spread, and the ROS values derived from the "ignition-to-instrument" and "video observation" methods agree most closely in this plot. Highly-instrumented plots 1 and 3 have greater variability in fire spread types and associated rate of spread (HIP 1 ROS derived from arrival at FBP was 0.23 m s^{-1} while the video-derived ROS was 0.40 m s^{-1}), the values for HIP 3 were 0.23 and 0.42 respectively. These observations imply that even in locations selected for uniform vegetation, microscale variations in plant spacing, type, and density can significantly affect overall fire spread and intensity and are best captured by discrete sensors spaced throughout the burn block.

Flame geometry measurements from observations of video footage are fraught with potential for error due to the difficulty in determining length scales in a two-dimensional image. Perhaps this challenge contributed to the variability in the observations for the burns discussed here. Camera images were somewhat clouded or otherwise compromised due to deposition of soot and debris on the windows or improper deployment. Integration of higher quality images would perhaps reduce the variability in this measurement.

The energy and heating levels presented in Fig. 5 and Table 4 suggest that S5 burned with generally lower intensity than L2G. However the within block variability (as indicated by standard deviation) suggests that S5 burned more uniformly than L2G. This is not necessarily supported by visual observations of fire images from the two burns, although it makes sense given that the within-block variability in ROS and the fire spread type variability for the HIPs in L2G are evident.

The integral of the heating curves, presented as the fire total, radiative and convective energy per unit area or FTE, FRE, and FCE, in Figs. 5(*e*) and 5(*f*) seem to indicate that the arrival and completion of flaming combustion can be indicated by significant upturn in the derivative of the energy curve. For example the fire arrival in Fig. 5(*f*) corresponds to the upward curvature in the FCE curve, while there is little change in the FRE curve. Secondly it seems significant that FCE exceeds FRE at the time of flame arrival. While this trend is not consistent across all sensors it is present in a large portion of them. It suggests that convective heating, while associated with rapid and large fluctuations in magnitude and duration of heating to cooling, is associated with the ignition of the vegetation. This observation suggests that while radiative heating contributes to the pyrolysis process, convective heating is the major driver of ignition, as should be expected for piloted ignition and that the convective events while short term are sufficient to lead to ignition of the irradiated vegetation.

Conclusions

The measurement of energy and mass transport in reacting systems is at best tenuous. In the context of wildland fire it is even more difficult and is associated with increased measurement uncertainty due to the fluctuating nature of the wildland fire environment. The data described here are part of the larger RxCADRE dataset, and build on what has historically been a limited data set of similar measurements. While the data presented in this work embody the low end of the spectrum of fire intensity, and are not as visually stimulating as what would be expected from heavier fuels (e.g. forests) which produce larger flames, they do represent an important first step in the building of a comprehensive dataset and will support future development of fire behavior, effects, and emissions models. Additionally, these data are integral to a better understanding of the contributions of radiative and convective heating to energy transport.

The measurements reported here are a first look at a subset of the RxCADRE dataset, but seem to suggest that quantification of fire intensity is improved when the number of sensors deployed on the ground is increased. Generally the data suggest that fires in short grass of relatively low stem density can be characterized by residence times of nominally 10 to 12 s. Air temperatures average 830°C with peak temperatures reaching nearly 1300°C. Heating values can reach 36 kW m^{-2}; however, the average total heating is approximately 20 kW m^{-2} with radiant and convective heating reaching 10 kW m^{-2}. Perhaps one of the most significant findings from this effort is that the magnitude of convective heating is on the order of radiant heating, and that it is associated with ignition of the vegetation. This suggests that both heating modes must be measured to adequately quantify the heating environment around fires in this vegetation type. Further analyses of all the data collected in this effort will likely provide additional information in this regard. As in any field campaign, several aspects regarding sensor setup and experiment methods could be improved, these include: the need for a distance and height metrics in camera field of view, measurement and recording of the height of the sensors relative to the vegetation height, the utility of overhead infrared imagery in developing continuous fire rate of spread information, the need for additional measurements and analysis of flame temperature data from very fine wire thermocouples and the need for additional measurements at high sampling rates to further characterize the temporal properties of the energy release from the flames. .

Acknowledgements

The financial support provided by the Joint Fire Science Program (Project #11-2-1-11) was crucial to this effort. The integrative and collaborative involvement of the many groups involved in the effort facilitated the deployment and collection of a large number of fire behavior packages. The leadership provided by R. Ottmar was also crucial to the project.

References

Albini FA (1996) Iterative solution of the radiation transport equations governing spread of fire in wildland fuel. *Combustion, Explosion, and Shock Waves* 32, 534–543. doi: 10.1007/BF01998575

Anderson HE (1969) Heat transfer and fire spread. USDA Forest Service Intermountain Forest and Range Experiment Station Research Paper INT-69. (Ogden, UT)

Anderson WR, Catchpole EA, Butler, BW (2010) Convective heat transfer in fire spread through fine fuel beds. *International Journal of Wildland Fire* 19, 284–298

Bryant R, Womeldorf C, Johnsson E, Ohlemiller T (2003) Radiative heat flux measurement uncertainty. *Fire and Materials* **27**, 209–222. doi:10.1002/fam.822

Butler BW (1993) Experimental measurements of radiant heat fluxes from simulated wildfire flames. In '12th International Conference of Fire and Forest Meteorology, Oct. 26-28, 1993. Jekyll Island, Georgia'. (Eds JM Saveland, J Cohen) Volume 1 pp. 104-111. (Society of American Foresters: Bethesda, MD)

Butler BW (2003) Field measurements of radiant energy transfer in full scale wind driven crown fires. In 'The Proceedings of the 6th ASME-JSME Thermal Engineering Joint Conference, AJTEC 2003: March 16-30, 20-03, Kohala Coast, Hawaii Island, Hawaii, USA'. (Japan Society of Mechanical Engineers: Tokyo)

Butler BW (2014) Wildland firefighter safety zones: a review of past science and summary of future needs. *International Journal of Wildland Fire* **23**, 295–308. doi:10.1071/WF13021

Butler BW, Cohen J, Latham DJ, Schuette RD, Sopko P, Shannon KS, Jimenez D, Bradshaw LS (2004) Measurements of radiant emissive power and temperatures in crown fires. *Canadian Journal of Forest Research* **34**, 1577–1587. doi:10.1139/x04-060

Butler BW, Cohen JD (1998) Firefighter safety zones: a theoretical model based on radiative heating. *International Journal of Wildland Fire* **8**, 73–77. doi**:**10.1071/WF9980073

Butler BW, Jimenez D (2009) In situ measurements of fire behavior. In '4th International Fire Ecology & Management Congress: Fire as a Global Process. Savannah, GA', 30 November—4 December, 2009. (Ed. S Rideout-Hanzak) The Association for Fire Ecology.

Finney MA, Cohen JD, Grenfel, IC, Yedinak KM (2010) An examination of fire spread thresholds in discontinuous fuel beds. *International Journal of Wildland Fire* **19**, 163–170. doi:10.1071/WF07177

Frankman D (2009) Radiation and convection heat transfer in wildland fire environments. Doctoral thesis. Brigham Young University, Department of Mechanical Engineering. (Provo, UT)

Frankman D, Webb BW, Butler BW (2010) Time-resolved radiation and convection heat transfer in combusting discontinuous fuel beds. *Combustion Science and Technology* **182**, 1–22. doi:10.1080/00102202.2010.486388

Frankman D, Webb BW, Butler BW, Jimenez D, Forthofer JM, Sopko P, Shannon KS, Hiers JK, Ottmar RD (2012*a*) Measurements of convective and radiative heating in wildland fires. *International Journal of Wildland Fire* **22**, 157–167. doi:10.1071/WF11097

Frankman D, Webb BW, Butler BW, Jimenez D, Harrington M (2012*b*) The effect of sampling rate on interpretation of the temporal characteristics of radiative and convective heating in wildland flames. *International Journal of Wildland Fire* **22**, 168–173. doi:10.1071/WF12034

Freeborn PH, Wooster MJ, Hao WM, Ryan CA, Nordgren BL, Baker SP, Ichoku C (2008) Relationships between energy release, fuel mass loss, and trace gas and aerosol emissions during laboratory biomass fires. *Journal of Geophysical Research* **113**, 17. doi: 10.1029/2007JD008679

Jimenez D, Forthofer JM, Reardon JJ, Butler BW (2007) Fire behavior sensor package remote trigger design. In: Butler BW, Cook W, eds. The fire environment—innovations, management, and policy. USDA Forest Service, Rocky Mountain Research Station, Proceedings RMRS-P-46CD. (Fort Collins, CO)

McCaffrey BJ, Heskestad G (1976) A robust bidirectional low-velocity probe for flame and fire application. *Combustion and Flame* **26**, 125–127. doi**:** 10.1016/0010-2180(76)90062-6

Morandini F, Silvani X (2010) Experimental investigation of the physical mechanisms governing the spread of wildfires. *International Journal of Wildland Fire* **19,** 570–582. doi:10.1071/WF08113

Omega Engineering Inc. N.d. Thermocouple response time. http://www.omega.com/temperature/Z/ThermocopuleResponseTime.html. (11 June 2014)

Ottmar, R, Hiers, JK, Clements, C, Butler, BW, Dickinson, MB, Potter, BE, O'Brien, J, Hudak, A, Rowell, EM, Zajkowski, TJ (In review) Measurements, datasets and preliminary result from the RxCADRE project. *International Journal of Wildland Fire*

Parent G, Acem Z, Lechene S, Boulet P (2010) Measurement of infrared radiation emitted by the flame of a vegetation fire. *International Journal of Thermal Sciences* **49,** 555–562. doi: 10.1016/j.ijthermalsci.2009.08.006

Pitts WM, Murthy AV, de Ris J, Filtz J, Nygard K, Smith D, Wetterlund I (2006) Round robin study of total heat flux gauge calibration at fire laboratories. *Fire Safety Journal* **41**, 459–475. doi:10.1016/j.firesaf.2006.04.004

Sacadura JF (2005) Radiative heat transfer in fire safety science. *Journal of Quantitative Spectroscopy and Radiative Transfer* **93**, 5–24. doi:10.1016/j.jqsrt.2004.08.011

Viskanta R (2008) Overview of some radiative transfer issues in simulation of unwanted fires. *International Journal of Thermal Sciences* 47, 1563–1570. doi: 10.1016/j.ijthermalsci.2008.01.008

Wooster MJ, Roberts G, Perry GLW, Kaufman YJ (2005) Retrieval of biomass combustion rates and totals from fire radiative power observations: FRP derivation and calibration relationships between biomass consumption and fire radiative energy release. *Journal of Geophysical Research* **110**, 24. doi: 10.1029/2005JD006318

Yedinak KM, Cohen JD, Forthofer JM, Finney MA (2010) An examination of flame shape related to convection heat transfer in deep-fuel beds. *International Journal of Wildland Fire* **19**, 171–178. doi: 10.1071/WF07143

Yedinak KM, Forthofer JM, Cohen JD, Finney MA (2006) Analysis of the profile of an open flame from a vertical fuel source. *Forest Ecology and Management* **234**, S89–S89. doi: 10.1016/j.foreco.2006.08.125

Table 1. General observations relating to sensors

Unit	FBP #	Associated video camera	Fire behavior package/camera comments	Fire comments
S5	18	9	Video failed	Head fire based on data.
	15	8	Temperature FBP failed	Video data suggest nearby flanking fire.
	3	8		Temperature suggest flame presence, video suggests flanking or low intensity heading fire.
	10	15, 14		Temperature and flux data suggest very low intensity fire—likely flanking.
	14	6, 14		Temperature and flux data suggest low intensity possibly flanking fire.
	7	14, 15		Temperature show fire present, flux data suggest very low intensity fire—likely flanking.
	5	15		Temperature and flux data clearly show fire was never nearby.
L2G HIP 1	22	19		Video shows head and flanking fire at FBP location.
	2	20		Video shows head fire, but FBP not in field of view.
	20	4		Video shows head fire at FBP location.
	3	14		Video shows head fire at FBP location.
	14	14	Temperature FBP failed	Data suggest fire was nearby, but did not directly reach FBP or was of very low intensity.
	19	12		Data suggest fire was nearby, but did not directly reach FBP or was of very low intensity.
	17	18		Data indicates it arrived at FBP but was low intensity.
HIP 2	21			
	6	7, GP2	Video failed	
	5	1		Video shows head fire at FBP location.
	13	1		Video shows head fire at FBP location.
	15	8, GP1		Video shows head fire at FBP location.
	7	3		Video shows flanking fire at FBP location.
	4	9		Video shows head fire at FBP location.
HIP 3	12	5		Video shows head and flanking fire at FBP location.
	10	6		Video shows spotty fire behavior at FBP location.
	16	16		Video blurry and FBP not in field of view.
	11	13		Video shows spotty fire behavior at FBP location.
	8	15		Video shows head and flanking fire at FBP location.
	18	17		Insufficient fuel to carry fire. Burn was patchy.

Table 2. Flame properties derived from video images

Unit	Camera	Flame height (m)	Flame depth (m)	Fire behavior package in camera field of view (Identification number)
S5	6	0.3-0.6	0.3-1	14
S5	8	0.3-0.6	0.3-1	3, 15
S5	9			18
S5	14	0.3-0.6	0.3-1	7, 10, 14
S5	15	0.3-0.6	1-1.5	5, 7, 10
Ave		0.45	0.75	
Std Dev		0.474	0.903	
L2G-HIP 1	4	0.3-1	1-1.5	
	12	0.3-1	0.3-1.5	
	14	1-1.5	1-1.5	
	18	0.3-1	0.3-1.5	
	19	0.3-1	1-1.5	
	20	1.5-1.8	1.5-3	
Ave		0.90	1.30	
Std Dev		1.044	1.46	
L2G-HIP 2	1	0.3-1	1.5-3	
	3	0.3-1	1.5-3	
	7			
	8	0.3-1	1.5-3	
	9	0.3-1	1.5-3	
Ave		0.60	2.30	
Std Dev		0.738	2.37	
L2G-HIP 3	5	0.3-1	1-1.5	
	6	0.3-1	1.5-3	
	13	0.3-1	1-1.5	
	15	0.6-1.2	1-1.5	
	16	0.6-1.2	1-1.5	
	17	0.6-1.2	1-1.5	
Ave		0.75	1.50	
Std Dev		0.85	1.51	

Table 3. Fire rate of spread (ROS)

Unit	Fire behavior package (FBP)	ROS based on FBP flame arrival time from ignition ($m\ s^{-1}$)	ROS based on transit time between sensors ($m\ s^{-1}$)	Camera # associated with fire behavior package[1]	ROS estimated from video images ($m\ s^{-1}$)
S5	18	0.28	0.28	9	0.56
	15	0.24	0.11		
	3	0.25	0.27	8	0.16
	10	0.23	0.20	14	0.12
	14	0.21	0.16	6	0.21
	7	0.23	0.35		
	5	N/A	N/A		
	Average	0.24	0.23		0.26
	Std Dev	0.02	0.09		0.20
L2G-HIP 1	22	0.32		4	0.24
	2	0.24		14	0.31
	20	0.25		19	0.44
	3	0.22		20	0.61
	14	0.22			
	19	0.1			
	17	--			
	Average	0.23			0.40
	Std Dev	0.07			0.16
L2G-HIP 2	21	0.33		1	0.34
	6	0.46		3	0.25
	5	0.47		8	0.38
	13	0.47		9	0.47
	15	0.44			
	7	0.45			
	4	0.48			
	Average	0.44			0.36
	Std Dev	0.05			0.09
L2G-HIP 3	12	0.25		5	0.46
	10	0.39		6	0.51
	16	0.16		13	0.38
	11	0.3		16	0.43
	8	0.27			
	18	0.16			
	9	0.1			
	Average	0.23			0.42
	Std Dev	0.10			0.07

[1]The associated FBP in column 2 was used for the ROS calculation.

Table 4. Energy measurements

Plot	FBP ID	Q_R (kW m^{-2})	Q_C (kW m^{-2})	Q_T (kW m^{-2})	E_F (kW m^{-2})	T_{air} (C)	t_{flame} (s)	$\overline{Q_R}$ (kW m^{-2})	$\overline{Q_C}$ (kW m^{-2})	$\overline{Q_T}$ (kW m^{-2})	FRE (kJ m^{-2})	FCE (kJ m^{-2})	FTE (kJ m^{-2})
S5	3	2.6	4.8	7.1	16.2	869	5	1.4	1.4	2.8	7	7	14
	5	1.1	1.3	2.2	3.8	284	–	–	–	–	–	–	–
	7	3.6	4.3	7.2	6.2	860	13	2.1	1.7	3.8	27.3	22.1	49.4
	10	3	2.9	5.3	17.7	575	20	1.9	0.8	2.7	38	16	54
	14	4.9	5	9.8	11.6	–	5	3.2	2.3	5.5	16	11.5	27.5
	15	5.5	9.5	14	23.9	–	8	3.6	4.5	8.1	28.8	36	64.8
	18	5.2	10.9	14.6	21.8	821	23	3.9	2.8	6.7	89.7	64.4	154.1
	Average	3.7	5.5	8.6	14.5	682	12.3	2.7	2.3	4.9	33.1	27.8	60.8
	Std Dev	*1.6*	*3.4*	*4.5*	*7.6*	*253*	*7.7*	*1*	*1.3*	*2.2*	*7.9*	*10.1*	*17.1*
L2G													
HIP 1	22	18.8	18.2	36.7	95.1	1159	21	11.1	7.8	19.3	143	118	261
	2	14.1	18.2	32.3	70.5	406	7	8.9	7.7	16.9	62.3	53.9	118.3
	20	7.5	5.6	12.5	13.2	644	16	4.7	1.1	5.9	75.2	17.6	94.4
	3	15.5	15.7	30.8	38.8	1280	14	9.1	4.8	14.1	127.4	67.2	197.4
	14	8.9	7.8	13.6	29.6	–	–	–	–	–	–	–	–
	19	1.6	7.6	8.8	7.9	804	4	2.2	2.9	0.7	8.8	11.6	2.8
	17	0.2	0.5	0.7	13.9	915	4	–	–	–	–	–	–
	Average	9.5	10.5	19.4	38.4	868	11	7.2	4.9	11.4	79.2	53.5	125.2
	Std Dev	*7*	*6.9*	*13.8*	*32.9*	*324*	*7*	*3.6*	*2.9*	*7.8*	*25.6*	*20.7*	*55.1*
HIP 2	21	3.5	10.5	12.9	15.3	755	10	2	3.1	5.2	20	31	52
	6	10.1	16.8	26.9	28.7	1106	4	6.9	8.1	15	27.6	32.4	60
	5	14.5	10.6	23.5	30.9	1125	10	9.7	4.1	13.9	97	41	139
	13	11.8	14.8	25.5	50.5	494	5	9.4	5.6	15	47	28	75
	15	9.3	13.5	22.1	34.3	857	7	6.8	7.4	14.2	47.6	51.8	99.4
	7	15.9	9.9	24	35.8	695	10	11.5	4.2	15.6	115	42	156

	4	9.1	5.3	13.2	21.4	629	4	7.6	0.8	8.7	30.4	3.2	34.8
	Average	10.6	11.7	21.2	31	809	7.1	7.7	4.8	12.5	55	34	89.4
	Std Dev	*4.1*	*3.8*	*5.7*	*11.3*	*237*	*2.9*	*3*	*2.5*	*4*	*8.7*	*7.2*	*11.3*
HIP 3	12	10.2	11	20	40.3	–	15	6.9	1.7	8.6	103.5	25.5	129
	10	16.3	14.1	30.2	80.9	425	6	10.2	2.5	12.8	61.2	15	76.8
	16	7.3	5.8	13.1	65	860	10	5	1.2	6.2	50	12	62
	11	9.9	7.4	16.2	35	576	17	6.9	1.8	8.6	117.3	30.6	146.2
	8	15.8	14	29.8	23.8	1013	16	10.1	3.2	13.3	161.6	51.2	212.8
	18	9.2	8.9	17.7	24.2	1003	14	5.3	3	8.3	74.2	42	116.2
	9	2.7	6.1	8.6	17.4	393	5	1.8	3.8	6.3	9	19	31.5
	Average	10.2	9.6	19.4	41	739	11.9	6.6	2.5	9.2	78.3	29.1	108.6
	Std Dev	*4.7*	*3.5*	*8.1*	*23.6*	*307*	*4.9*	*3*	*0.9*	*2.8*	*14.5*	*4.6*	*13.9*
L2G	Mean	10.1	10.6	20	36.8	805	10	6.8	3.8	10.4	67.7	37.5	103.8
	Std Dev	*5.2*	*4.8*	*9.3*	*23.4*	*275*	*5.3*	*3.4*	*2.5*	*5.3*	*58*	*34.8*	*90.7*

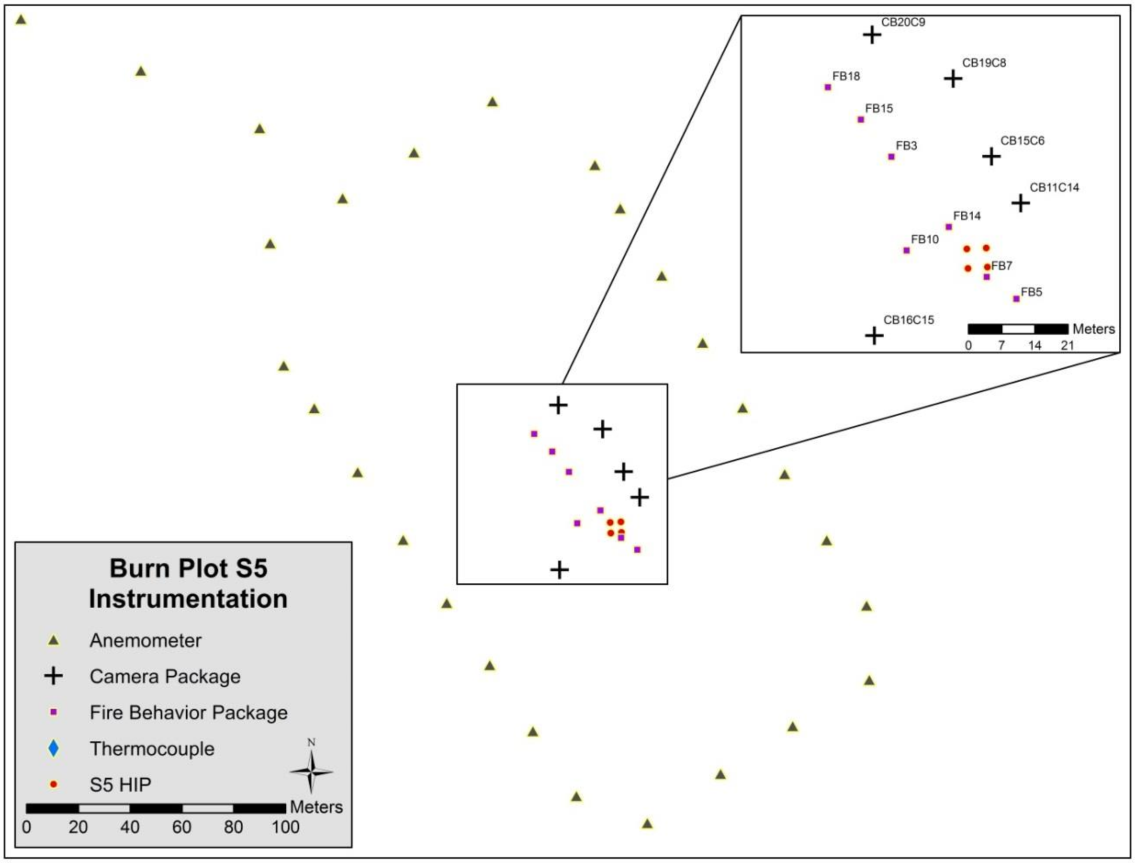

Fig. 1. Sensor layout for burn block S5.

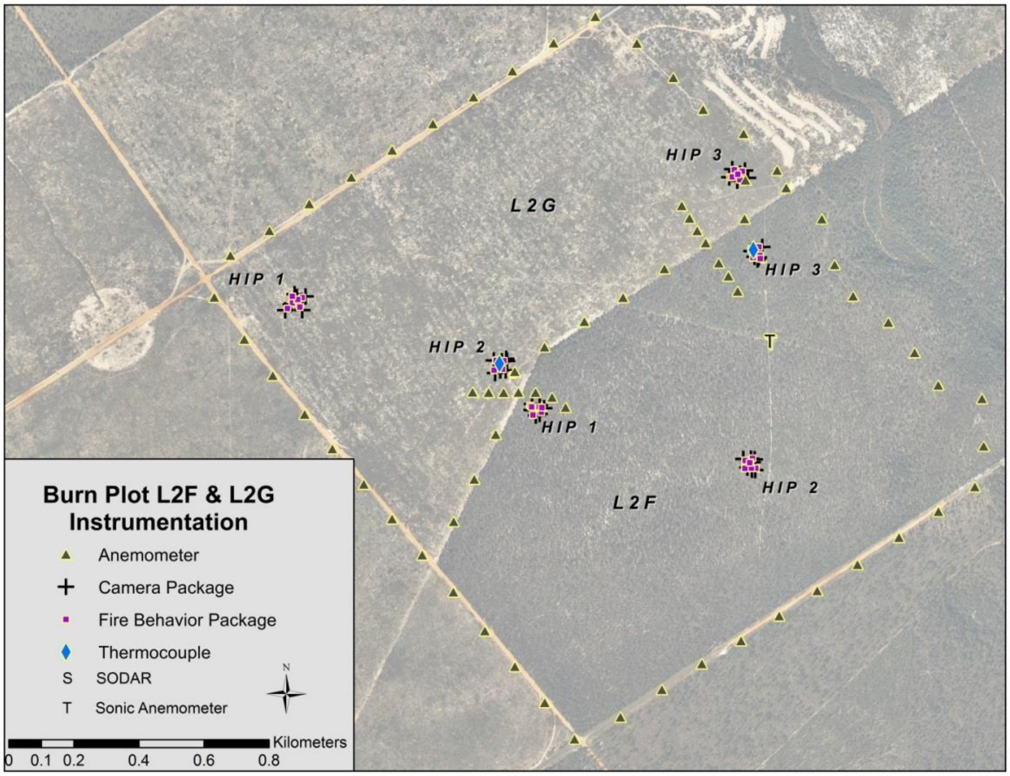

Fig. 2. Sensor layout and general location of burn blocks L2G and L2F.

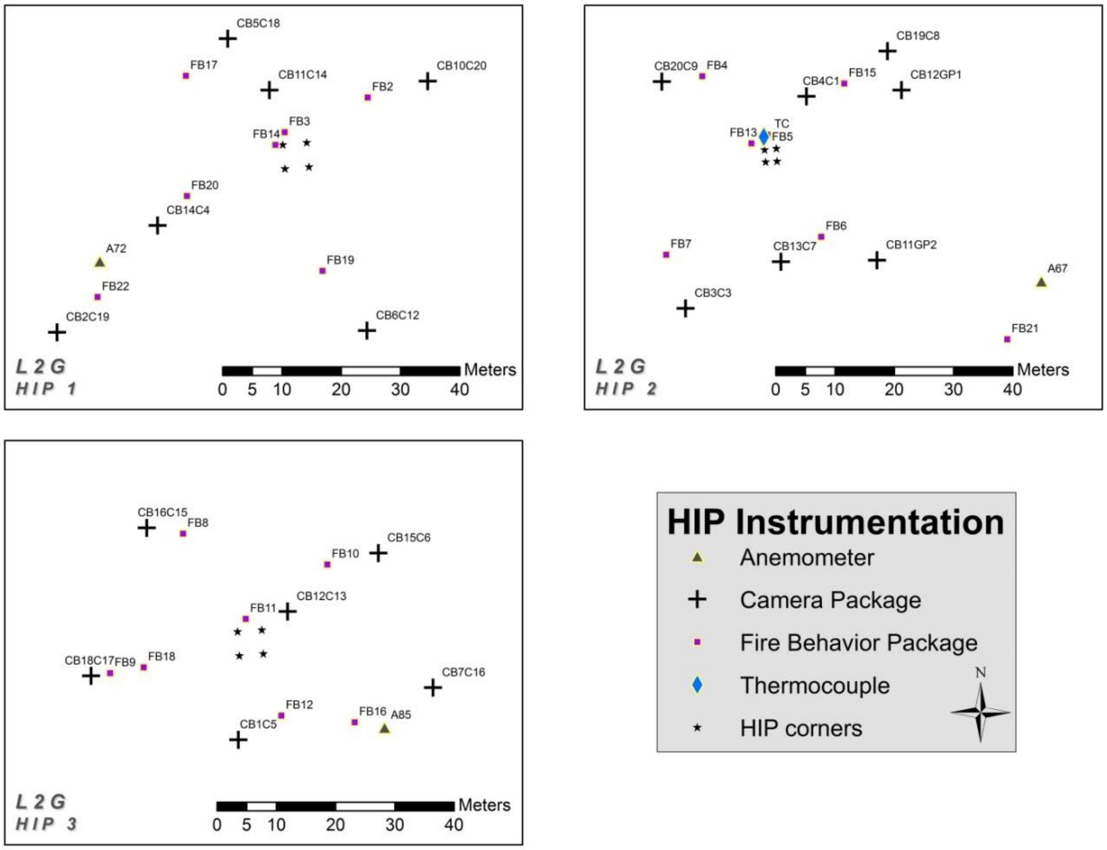

Fig. 3. Highly-instrumented plot (HIP) sensor locations for burn unit L2G.

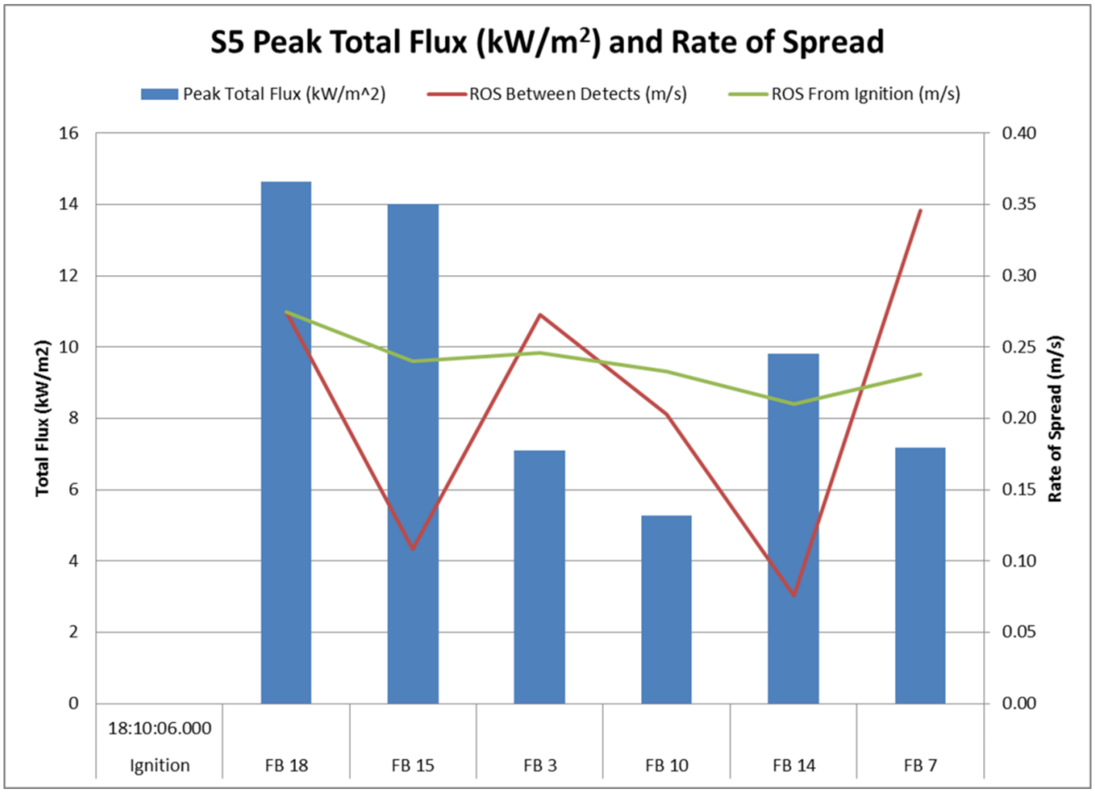

Fig. 4. Example of the variability in rate of spread as fire moves between sensors. Blue bars represent total measured energy at sensor, red line presents rate of spread between sensors calculated from time of arrival at each sensor and distance between sensors, green line represents overall rate of spread since fire was ignited to the sensor location.

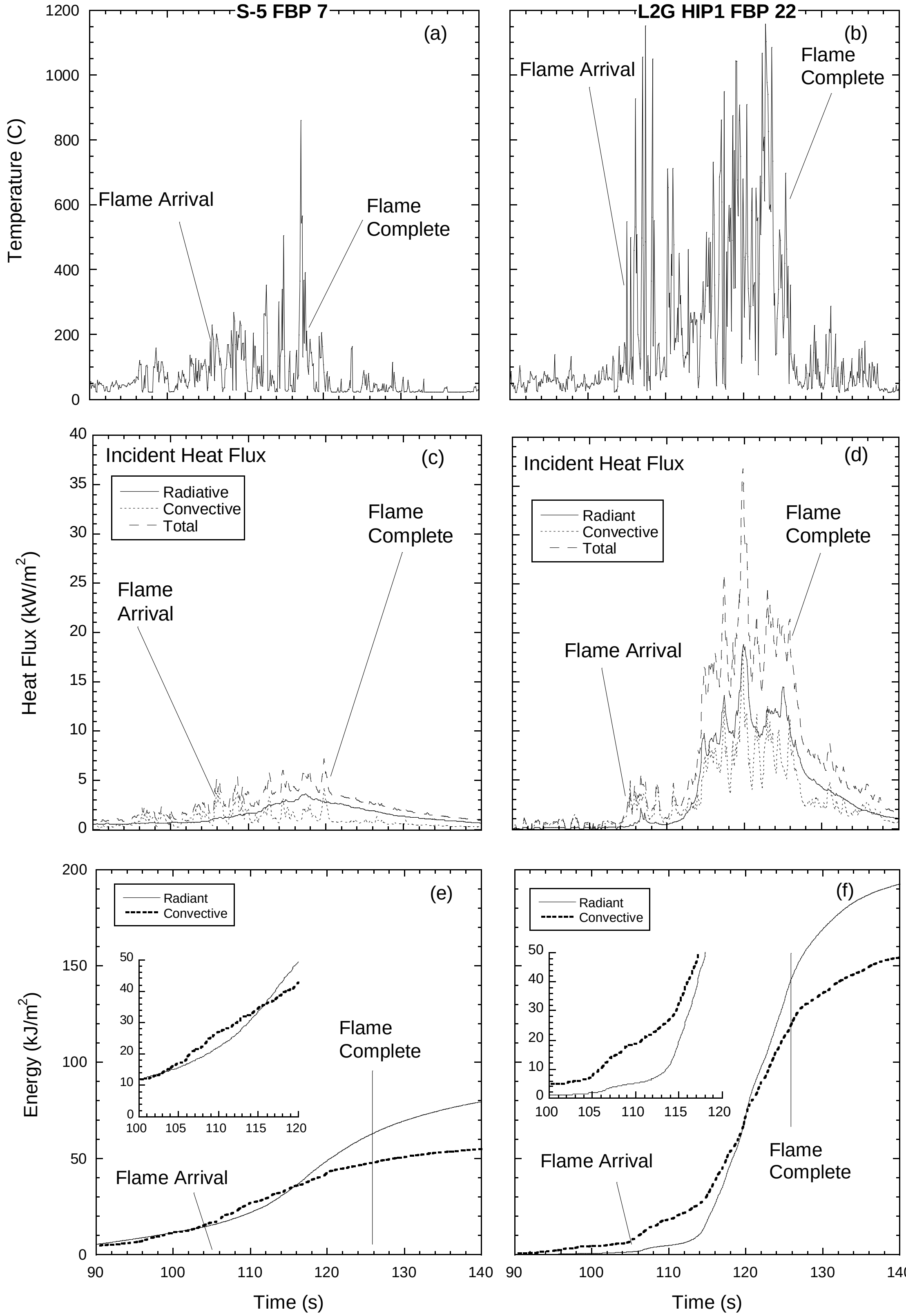

Fig. 5. Selected measurements from S5 (left column) and L2G HIP 1 (right column).